

# Online Vectorized HD Map Construction using Geometry

Zhixin Zhang<sup>1</sup>, Yiyuan Zhang<sup>2</sup>, Xiaohan Ding<sup>3</sup>, Fusheng Jin<sup>1\*</sup>, Xiangyu Yue<sup>2</sup>

<sup>1</sup>Beijing Institute of Technology    <sup>2</sup>The Chinese University of Hong Kong    <sup>3</sup>Tencent AI Lab

zhangzhixin@bit.edu.cn, yiyuanzhang.ai@gmail.com, xyyue@ie.cuhk.edu.hk

<https://invictus717.github.io/GeMap/>

## Abstract

The construction of online vectorized High-Definition (HD) maps is critical for downstream prediction and planning. Recent efforts have built strong baselines for this task, however, shapes and relations of instances in urban road systems are still under-explored, such as parallelism, perpendicular, or rectangle-shape. In our work, we propose GeMap (**Geometry Map**), which end-to-end learns Euclidean shapes and relations of map instances beyond basic perception. Specifically, we design a geometric loss based on angle and distance clues, which is robust to rigid transformations. We also decouple self-attention to independently handle Euclidean shapes and relations. Our method achieves new state-of-the-art performance on the NuScenes and Argoverse 2 datasets. Remarkably, it reaches a 71.8% mAP on the large-scale Argoverse 2 dataset, outperforming MapTR V2 by +4.4% and surpassing the 70% mAP threshold for the first time. Code is available at <https://github.com/cnzzx/GeMap>.

## 1. Introduction

Vectorized HD maps provide sparse and structured environmental information for autonomous vehicles and have been widely adopted in downstream tasks, such as trajectory forecasting [3, 17, 46] and planning [5, 32]. Online Vectorized HD Map Construction can significantly reduce the need for labor-intensive annotations and facilitate real-time updates in autonomous driving [4, 14, 18].

With the development of Bird’s-Eye-View (BEV) representation, online HD map construction has achieved significant advancements [9, 16, 19]. Early works [11, 27, 30, 42] formulate HD Map construction as a dense prediction task. However, these methods generate maps in image format, which is redundant for representing sparse map instances. Then, a more compact map formulation was introduced to

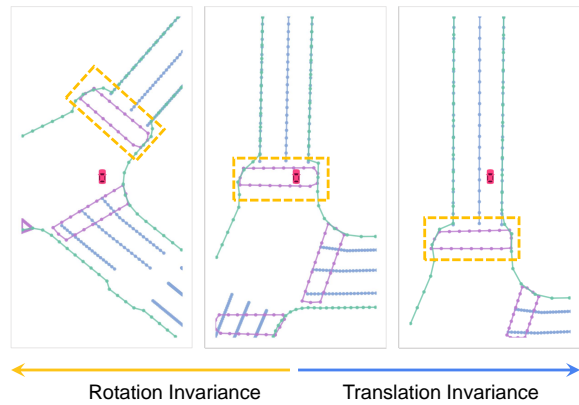


Figure 1. **Invariant Geometric Properties.** As the ego vehicle moves, after rotation ( $\leftarrow$ ) or translation ( $\rightarrow$ ), the shape of this crossing and relationship (perpendicular) between other lanes stays unchanged, which indicates the invariant property of geometry to rigid transformations.

minimize redundancy, albeit at the cost of adding time-consuming post-processing steps [14]. In response to this, recent works [4, 18, 21, 31] attempt to construct vectorized HD maps end-to-end to avoid extensive post-processing. These methods typically sample points from map instances and represent each instance as a polyline [4, 18, 21] or parameterized curve [31].

We observe that urban road systems exhibit significant geometric characteristics, such as parallel lanes, perpendicular crossings, equal lane widths, *etc.* However, these geometric properties of shapes and relations between map instances have not been fully explored. Meanwhile, there are two notable limitations among existing methods [4, 18, 21, 31] which can be alleviated by leveraging these geometric properties. **1)** As the ego-vehicle moves, instances experience rotations and translations, as depicted in Figure 1. However, the polylines and parameterized curve representations employed in prior research, which rely on the absolute coordinates of points, are inherently sensitive to these rotational and translational changes [7, 31]. **2)** Geometric prop-

\*Corresponding author

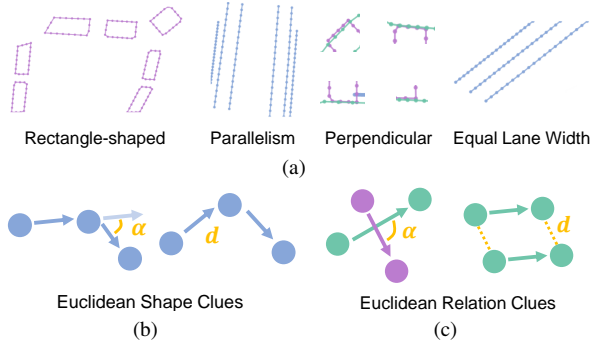


Figure 2. **Geometric properties and G-Representation.** (a) Geometry in urban road system. For example, pedestrian crossings are near rectangular intersections and are always vertical to road boundaries. (b) (c) We propose to utilize angles and distances to model local geometry in a map instance and between different instances, denoted as Euclidean Shape Clues (§ 3.3.1) and Euclidean Relation Clues (§ 3.3.2), respectively. Note that included angles and distances between map instances are invariant to positional and directional changes of an ego vehicle.

erties widely exist in driving scenarios such as rectangle shape, parallelism, and perpendicular relationships, as illustrated in Figure 2a. Incorporating these properties could significantly enhance HD map construction. However, the vanilla attention mechanism struggles to effectively learn diverse shape and relation geometry due to objective conflicts, as detailed in § 3.5.

To address the above two limitations, we introduce a geometric representation that captures shapes of individual map instances and relations between different instances as illustrated in Figure 2b and 2c, referred to as **G-Representation**. It enhances the vanilla representation of map instances by incorporating a translation- and rotation-invariant representation that effectively leverages instance geometry. The local structures of map features are encoded using *displacement vectors*. These vectors are computed from the absolute coordinates of polyline points to effectively represent the relative positions and orientations of adjacent points. To quantify these features within Euclidean space, we employ both the *magnitudes* of the displacement vectors and the *angles* formed between these vectors. Based on G-Representation, we propose **Euclidean Shape Clues** to represent the shapes of individual map instances and **Euclidean Relation Clues** to represent the inter-instance relations in Euclidean space.

G-Representation addresses the abovementioned two limitations in an elegant way. **1)** By concentrating on the relative relationships between points within and across map instances, it inherently attains translation and rotation invariance. This enhances its robustness against variations in data collection and equips it to effectively handle different coordinate systems. **2)** It captures the inherent geometry in urban road systems. For instance, in Euclidean space, the

geometric representation of parallel lanes is indicated by an almost negligible angle between their displacement vectors, approaching zero.

Building upon G-Representation, we propose a framework named **GeMap** for HD map construction. It includes a BEV encoder to extract BEV features from multi-view input images and a geometry-decoupled decoder with a refined focus on geometric aspects. Specifically, we adapt the attention mechanism [37] and propose **Geometry-Decoupled Attention (GDA)**. GDA sequentially applies attention to queries belonging to the same instance and attention to queries across different instances. This can significantly boost the learning of key points of shapes and relations between map instances. Furthermore, we propose an objective function named *Euclidean Loss* to optimize G-Representation. Specifically, we transform the conventional polylines of the ground truth map into our G-Representation. In this way, the model gets optimized to better understand the magnitude of displacement vectors and the angles between them, thereby facilitating a more effective learning of geometric properties.

Experiments on NuScenes and Argoverse 2 datasets demonstrate the effectiveness of GeMap. We reach new state-of-the-art performances on both datasets. With camera images only, GeMap achieves 69.4% and 71.8% mAP on the Nuscenes and Argoverse 2, respectively.

Our contributions are summarized as follows.

- We propose G-Representation which harnesses critical geometric properties of rotational and translational invariance in autonomous driving scenes, opening up new research avenues within the field.
- We introduce GeMap, an innovative framework incorporating geometry-decoupled attention and Euclidean Loss function, specifically designed to enhance geometric learning capabilities in Online HD Map.
- GeMap achieves new state-of-the-art results in HD map construction on the NuScenes and Argoverse 2 datasets, notably surpassing the 70% mAP on the large-scale Argoverse 2 dataset for the first time.

## 2. Related Work

### 2.1. Online HD Map Construction

Traditionally, HD map construction has required labor-intensive manual or semi-automatic annotations [11, 28]. To streamline this, recent studies [16, 26, 29, 30, 45] have focused on online construction, approaching HD maps as a dense prediction challenge. Innovations such as MetaBEV [8] aim to mitigate sensor issues, while MVNet [40] uses historical data for improved semantic consistency. The trend towards automatic vectorization of HD maps is spearheaded by works such as HDMaPNet [14], which fuses camera and LiDAR inputs in BEV

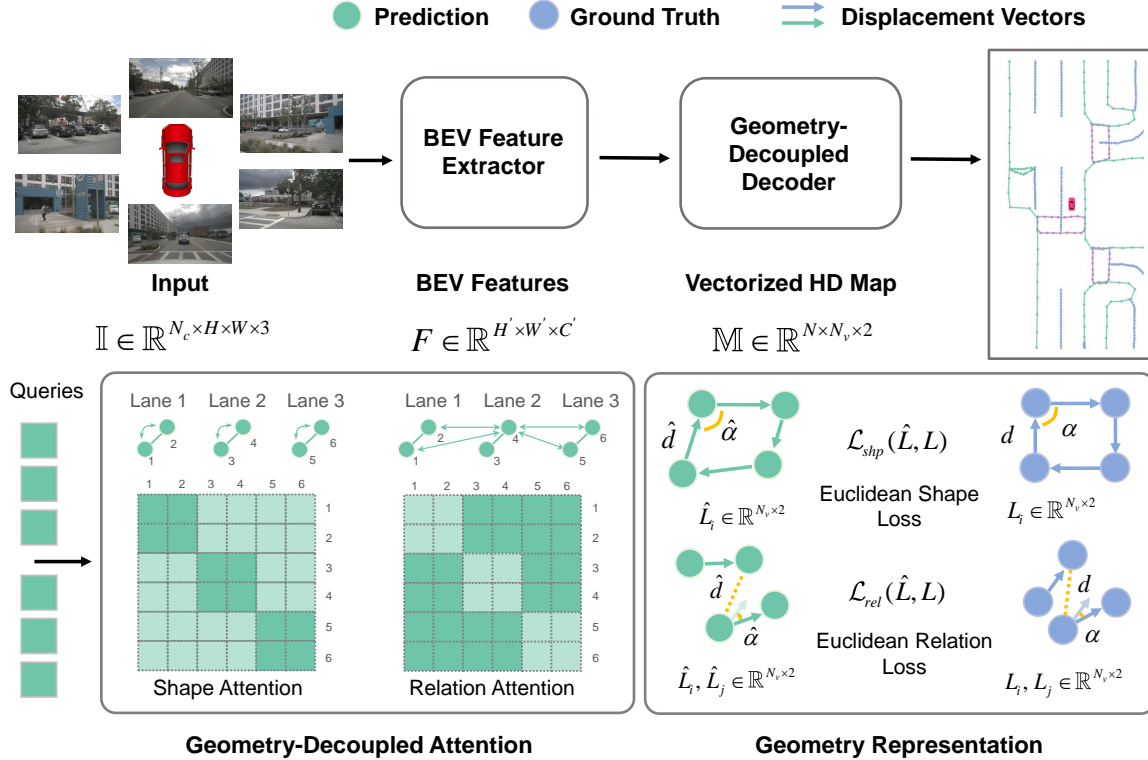


Figure 3. Illustration of our framework. First, PV images are transformed into BEV features, then a geometry-decoupled decoder outputs the vectorized HD Map. In each block of the decoder, queries are first processed by Euclidean shape and relation attention, which focuses on geometric relevance. Finally, predictions are enhanced in G-Representations by shape and relation constraint.

space and is advanced by end-to-end solutions such as VectorMapNet [21] and MapTR [18], leveraging Transformer-based models. StreamMapNet [43] and PivotNet [4] build upon this, modifying attention mechanisms for better performance. Our contribution starts from the strengths of the Transformer architecture, optimizing it with a decoupled self-attention block for enhanced geometric processing.

## 2.2. Cross-view BEV Learning

In autonomous driving systems, the conversion of Perspective View (PV) camera images into a unified BEV space is a significant challenge. While previous studies such as [15, 30] use depth estimation from monocular images for this transformation, others [2, 16, 23] have developed PV-to-BEV conversion methods without explicit depth details. For example, GKT [2] employs a geometric-guided kernel, and BEVFormer [16] uses deformable attention for the BEV conversion. However, these methods can distort shapes and geometric relations, leading to inaccuracies. Our approach integrates geometric supervision into prediction, addressing these geometric inconsistencies while acknowledging the value of depth information.

## 2.3. Geometric Instance Modeling

HD maps, depicting diverse geometric features such as pedestrian crossings and lane boundaries, present vector-

ization challenges. Traditional vectorization approaches model these features as polylines [18, 21, 33, 38] or polynomial curves [6, 31, 34, 36], with some incorporating Bézier Curves for improved fitting [6, 31]. However, such methods often overlook geometric properties including shapes, parallelism, *etc.* Research on geometric loss has mainly addressed rasterization-based shape [36, 44] or edge loss [18], and fails to preserve cross-instance relationships. PivotNet [4] offers an architectural advancement with its line-aware point decoder, yet it still does not fully address the complexity of instance geometry.

Given the current under-exploration of diverse geometries in shape and relation, we propose utilizing Euclidean shape and relation losses and decoupling the traditional self-attention module to empower the model with a more robust understanding of instance geometry.

## 3. Method

### 3.1. Preliminary

The architecture of our method is illustrated in Figure 3. Input images are denoted by  $\mathbb{I} = \{\mathbf{I}_i\}_{i=1}^{N_c}$ , where  $\mathbf{I}_i \in \mathbb{R}^{H \times W \times 3}$  and  $N_c$  is the sample number. Output is a set of  $N$  map instances  $\mathbb{M} = \{\mathbf{L}_i\}_{i=1}^N$ , where each map instance is represented by a polyline  $\mathbf{L}_i \in \mathbb{R}^{N_v \times 2}$ , *i.e.*, an ordered sequence of  $N_v$  two-dimensional points. As shown

in Table 3, the commonly adopted pipeline comprises three steps. **1)** A BEV feature extractor processes the multi-view images. **2)** The extracted BEV features are fed into a map decoder, which predicts the map instances based on the BEV features. **3)** To optimize the pipeline, the predicted map instances are compared against the ground truth. Beyond point-to-point comparison, G-representations of predictions and the ground truth are computed and the difference is measured by  $L^1$  loss.

### 3.2. Architecture Overview

**BEV Feature Extractor.** A shared vision backbone in different views and parameterized PV-to-BEV transformation network are employed to aggregate features from various perspectives. In our default configuration, we utilize ResNet [10] as the PV backbone and GKT [2] as the PV-to-BEV transformation network.

**Geometry-Decoupled Decoder.** We adopt a Transformer decoder to predict polylines. The decoder obtains  $N \times N_v$  queries that represent points and processes them via self-attention and aggregate BEV features via deformable cross-attention [47]. Finally, a prediction head is used to convert queries to polylines  $\{\hat{L}_i\}_{i=1}^N$ . We utilize a multi-layer perceptron as the polyline prediction head.

**Geometric Loss.** For training, we convert both the predicted polylines and ground truth into the proposed G-Representation. Based on that, we let the model optimize the predicted lengths of displacement vectors and angles between displacement vectors to match the ground truth.

In the following subsections, we first introduce Geometric Representation in § 3.3 since it is the core of our framework. Based on that, we introduce Geometric Loss in § 3.4 and Geometry-Decoupled Decoder in § 3.5, respectively.

## 3.3. Geometric Representation

### 3.3.1 Euclidean Shape Clues

We first introduce the representation of shapes of individual map instances. For each instance, we describe the local geometry with displacement vectors between neighboring points. The displacement vectors are computed as

$$\mathbf{v}_u^i = \mathbf{L}_{i,u+1} - \mathbf{L}_{i,u} \quad (u \in \{1, 2, \dots, N_v\}), \quad (1)$$

where we define  $\mathbf{L}_{i,N_v+1} := \mathbf{L}_{i,1}$  to unify the geometric formulation of closed and open polylines.

These displacement vectors are sufficient to represent the shape of a map instance and such a representation is invariant to rigid transformations. However, we would like to note that this representation is vulnerable to rotations, which might prevent the model from learning robust geometry. To solve this problem, we propose to represent the shape with lengths of displacement vectors and angles between consecutive displacement vectors, as illustrated in

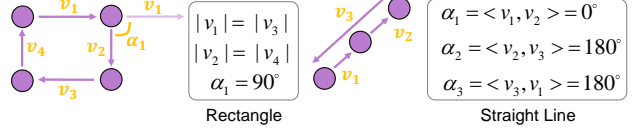


Figure 4. Euclidean shape clues. Lengths of displacement vectors and angles between neighboring vectors consist of shape clues and are utilized to compute shape loss. The right part shows how to connect Euclidean shape clues to shape geometry.

Figure 4. Specifically, the  $i$ -th instance is denoted by  $N_v$  angle values and  $N_v$  distance values. Let  $u$  be the index, the  $u$ -th angle value and distance value of the  $i$ -th instance are computed as

$$\alpha_u^i = \langle \mathbf{v}_u^i, \mathbf{v}_{u+1}^i \rangle, \quad d_u^i = \|\mathbf{v}_u^i\|_2, \quad (2)$$

where  $\langle \cdot \rangle$  denotes the angle between two vectors.

The proposed representation inherently captures common geometric patterns, such as parallelism, right angles, and proper line width, by translating them into corresponding numerical patterns within this representation. For example (Figure 4), a rectangle is characterized by one  $90^\circ$  angle and equal lengths of opposite displacement vectors; in addition, a straight line is represented by a  $0^\circ$  angle.

### 3.3.2 Euclidean Relation Clues

Having highlighted the translation and rotation invariance of G-Representation and its advantages in representing the geometric shapes of individual map instances, we further introduce its ability to capture the relations between two map instances, *e.g.*, parallelism and perpendicularity between two instances in the Euclidean space. Specifically,

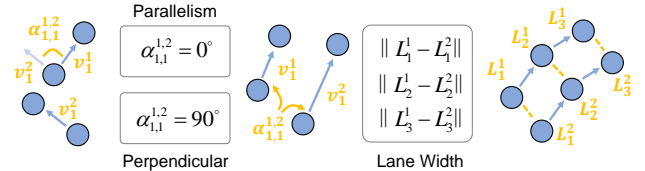


Figure 5. Euclidean relation clues. Distances between pairs of points and angles between pairs of displacement vectors indicate relation clues. Such relation clues are more superficially connected to Euclidean relation geometry as shown in the right part.

given the vanilla representations and displacement vectors of the  $i$ -th and  $j$ -th map instance, we represent the relation between instance  $i$  and  $j$  with 1) angles between each pair of their respective displacement vectors, and 2) distances between each pair of their points, as illustrated in Figure 5. Formally,

$$\alpha_{u,v}^{i,j} = \langle \mathbf{v}_u^i, \mathbf{v}_v^j \rangle, \quad d_{u,v}^{i,j} = \|\mathbf{L}_{i,u} - \mathbf{L}_{j,v}\|_2. \quad (3)$$

This representation is also translation- and rotation-invariant. Similar to Euclidean Shape Clues, it inherently



captures common relations between map instances by translating them into corresponding numerical patterns. For example, Figure 5 shows that the perpendicular relation can be directly represented by a 90° angle, and the distance between two parallel polylines, which may correspond to the width of a lane, is naturally represented by point-to-point distances.

### 3.4. Euclidean Loss and Objectives

We transform both the ground truth data and the model’s predicted polylines from their original format into G-Representation. This conversion allows the model to independently optimize the angles between displacement vectors and the distances between points to more accurately align with the ground truth. The proposed Euclidean Loss is composed of two parts that measure how accurately the model predicts the shape of individual map instances and the inter-instance relations, respectively, which are denoted by  $\mathcal{L}_{\text{shp}}$  and  $\mathcal{L}_{\text{rel}}$ . The Euclidean Loss can be computed as the following:

$$\mathcal{L}_{\text{Euc}} = \lambda_1 \cdot \mathcal{L}_{\text{shp}} + \lambda_2 \cdot \mathcal{L}_{\text{rel}}. \quad (4)$$

Specifically,

$$\begin{aligned} \mathcal{L}_{\text{shp}} &= \sum_{i=1}^N \sum_{j=1}^{N_v} |\hat{d}_j^i - d_j^i| + \ell(\hat{\alpha}_j^i, \alpha_j^i), \\ \mathcal{L}_{\text{rel}} &= \sum_{i=1}^N \sum_{j>i}^N \sum_{u=1}^{N_v} |\hat{d}_u^{i,j} - d_u^{i,j}| + \sum_{v=1}^{N_v} \ell(\hat{\alpha}_{u,v}^{i,j}, \alpha_{u,v}^{i,j}), \end{aligned} \quad (5)$$

where  $\ell(\cdot)$  is a special loss function based on  $L^1$  loss. We avoid using the inverse trigonometric function to directly compute the angles, but use sine and cosine values instead:

$$\ell(\hat{\alpha}, \alpha) = |\cos(\hat{\alpha}) - \cos(\alpha)| + |\sin(\hat{\alpha}) - \sin(\alpha)|. \quad (6)$$

Following the common practice [18, 43], we also use focal loss [20] for classification denoted by  $\mathcal{L}_{\text{cls}}$ . For polyline regression, we adopt point-to-point loss and edge direction loss, denoted by  $\mathcal{L}_{\text{pts}}$  and  $\mathcal{L}_{\text{dir}}$  respectively. Following [19, 31], we further adopt segmentation-based loss  $\mathcal{L}_{\text{seg}}$  and depth estimation loss  $\mathcal{L}_{\text{dep}}$  (Details in Appendix). The overall loss function can be written as:

$$\begin{aligned} \mathcal{L} &= \lambda \cdot \mathcal{L}_{\text{Euc}} + \beta_1 \cdot \mathcal{L}_{\text{cls}} + \beta_2 \cdot \mathcal{L}_{\text{pts}} \\ &\quad + \beta_3 \cdot \mathcal{L}_{\text{dir}} + \beta_4 \cdot \mathcal{L}_{\text{seg}} + \beta_5 \cdot \mathcal{L}_{\text{dep}}. \end{aligned} \quad (7)$$

We would like to note that  $\mathcal{L}_{\text{seg}}$  and  $\mathcal{L}_{\text{dep}}$  are optional. We also experiment with a simpler objective function to evaluate the effect of our main contribution alone, rather than compete with the recent powerful baselines. That is,

$$\mathcal{L}' = \lambda \cdot \mathcal{L}_{\text{geo}} + \beta_1 \cdot \mathcal{L}_{\text{cls}} + \beta_2 \cdot \mathcal{L}_{\text{pts}} + \beta_3 \cdot \mathcal{L}_{\text{dir}}. \quad (8)$$

The most relevant hyperparameters to our contributions include  $\lambda$ ,  $\lambda_1$ , and  $\lambda_2$ , whose effects on the model performances are evaluated in § 4.5.

### 3.5. Geometry-Decoupled Decoder

In the Transformer decoder, we obtain the  $N \times N_v$  fused queries by adding  $N$  instance queries to  $N_v$  point queries, which is suggested in [18]. We denote input tokens by  $\mathbf{E} \in \mathbb{R}^{N_A \times D}$ , where  $D$  is the feature dimension and  $N_A = N \cdot N_v$  is the number of fused queries. Intuitively, each fused query corresponds to a point on a predicted map instance. Self-Attention (SA) is formulated by

$$\text{SA}(\mathbf{E}, \mathbf{M}) = \text{Softmax} \left( \frac{(\mathbf{E}\mathbf{W}^q)(\mathbf{E}\mathbf{W}^k)^\top}{\sqrt{D_k}} \odot \mathbf{M} \right) \mathbf{E}\mathbf{W}^v, \quad (9)$$

where  $\mathbf{W}^q, \mathbf{W}^k, \mathbf{W}^v \in \mathbb{R}^{D \times D_k}$  are linear projection matrices,  $\mathbf{M} \in \mathbb{R}^{N_A \times N_A}$  is the attention mask, and  $\odot$  is the Hadamard product. The vanilla SA computes relations between every pair of tokens.

Nevertheless, the geometry of shape and relation pertains to distinct subsets of tokens. For any given map instance, its shape is intimately related to tokens representing that instance’s points. *Precise shape geometry capture requires the model to discern token correlations specific to an instance while avoiding interference from tokens of unrelated instances.* Conversely, for relation geometry modeling, it is beneficial to isolate token correlations that span across different instances, rather than those confined within a single instance.

Therefore, we present Geometry-Decoupled Attention (GDA). First, we multiply a binary mask  $\mathbf{M}$  to the computed attention map so that the tokens of a map instance are aggregated according to the tokens within the same map instances only, which allows the model to adjust points’ positions according to learned shape geometry. Denote the index of map instance that the  $i$ -th token belongs to as  $\mathcal{I}_i$ . For example, tokens  $1, 2, \dots, N_v$  belong to the first instance so that  $\mathcal{I}_1, \mathcal{I}_2, \dots, \mathcal{I}_{N_v} = 1$ . Tokens  $N_v+1, N_v+2, \dots, 2 \cdot N_v$  belong to the second instance so that  $\mathcal{I}_{N_v+1}, \mathcal{I}_{N_v+2}, \dots, \mathcal{I}_{2N_v} = 2$ . With this notation, the binary mask  $\mathbf{M}$  can be simply constructed by

$$\mathbf{M}_{i,j}^{\text{shp}} = \begin{cases} 1 & , \mathcal{I}_i = \mathcal{I}_j \\ 0 & , \mathcal{I}_i \neq \mathcal{I}_j \end{cases}. \quad (10)$$

The second attention is expected to model relations between tokens of different map instances. The attention mask is given by

$$\mathbf{M}_{i,j}^{\text{rel}} = \begin{cases} 1 & , \mathcal{I}_i \neq \mathcal{I}_j \\ 0 & , \mathcal{I}_i = \mathcal{I}_j \end{cases}. \quad (11)$$

## 4. Experiments

### 4.1. Experimental Setups

**Datasets.** To evaluate our method, we conduct experiments on the NuScenes dataset [1], a widely recognized large-scale autonomous driving dataset that includes 1,000 scenes

Table 1. Comparison on the NuScenes dataset and our method reaches a new state-of-the-art performance. "EB0", "R50", "PP", "Sec", denote EfficientNet-B0 [35], ResNet50 [10], PointPillars [12], SECOND [41] respectively. Methods with two backbones utilize both camera and LiDAR inputs. "Seg. Loss" denotes whether any segmentation-based loss is adopted. The best result is highlighted in **bold**. We reproduce different methods on a single RTX3090 GPU to test FPS for fair comparison.

Methods	Backbone	Seg. Loss	AP <sub>div</sub> (↑)	AP <sub>ped</sub> (↑)	AP <sub>bnd</sub> (↑)	mAP(↑)	FPS(↑)
VectorMapNet [ICML'23] [21]	R50		42.5	51.4	44.1	46.0	5.3
MapTR [ICLR'23] [18]	R50		59.8	56.2	60.1	58.7	<b>19.8</b>
GeMap [Ours]	R50		<b>65.1</b> ↑ 5.3	<b>59.8</b> ↑ 3.6	<b>63.2</b> ↑ 3.1	<b>62.7</b> ↑ 4.0	15.6
HMapNet [ICRA'22] [14]	EB0	✓	14.4	21.7	33.0	23.0	0.7
PivotNet [ICCV'23] [4]	R50	✓	58.8	53.8	59.6	57.4	-
BeMapNet [CVPR'23] [31]	R50	✓	66.7	62.6	65.1	64.8	6.6
MapTRv2 [Arxiv'23] [19]	R50	✓	68.3	<b>68.1</b>	69.7	68.7	<b>15.0</b>
GeMap [Ours]	R50	✓	<b>69.8</b> ↑ 1.5	67.1	<b>71.4</b> ↑ 1.7	<b>69.4</b> ↑ 0.7	13.3
HMapNet [ICRA'22] [14]	EB0 & PP		29.6	16.3	46.7	31.0	-
VectorMapNet [ICML'23] [21]	R50 & PP		60.1	48.2	53.0	53.7	-
MapTR [ICLR'23] [18]	R50 & Sec		62.3	55.9	69.3	62.5	-
GeMap [Ours]	R50 & Sec		<b>66.3</b> ↑ 4.0	<b>62.2</b> ↑ 6.3	<b>71.1</b> ↑ 1.8	<b>66.5</b> ↑ 4.0	6.8

Table 2. Following BeMapNet [31], we also compare our methods on the NuScenes dataset under different weather conditions.

Methods	Backbone	Seg. Loss	mAP <sub>sun</sub> (↑)	mAP <sub>cloud</sub> (↑)	mAP <sub>rainy</sub> (↑)	mAP <sub>avg</sub> (↑)	FPS(↑)
VectorMapNet [ICML'23] [21]	R50		43.8	44.1	36.6	41.5	5.3
MapTR [ICLR'23] [18]	R50		62.1	60.5	52.8	58.4	<b>19.8</b>
GeMap [Ours]	R50		<b>66.0</b> ↑ 3.9	<b>64.3</b> ↑ 3.8	<b>54.4</b> ↑ 1.6	<b>61.5</b> ↑ 3.1	15.6
BeMapNet [CVPR'23] [31]	R50	✓	67.3	67.5	56.6	63.8	6.6
GeMap [Ours]	R50	✓	<b>73.1</b> ↑ 5.8	<b>71.0</b> ↑ 3.5	<b>59.3</b> ↑ 2.7	<b>67.8</b> ↑ 4.0	<b>13.3</b>

captured by six RGB cameras with a 360-degree field of view, and provides precise annotations from LiDAR point clouds for HD map construction. For comparability with prior research [14, 18], we focus on three static categories of map instances: pedestrian crossings, lane dividers, and road boundaries. With dataset splits provided by BeMapNet [31], we also evaluate our methods under three weather conditions: sunny, cloudy, and rainy. Additionally, we used the Argoverse 2 dataset [39] as another benchmark, which consists of approximately 108,000 frames, each providing images from seven cameras.

**Metrics.** We evaluate the performance of our method using the widely adopted metric of Average Precision (AP) [14, 18]. Specifically, we categorize a prediction as a True Positive if the Chamfer Distance between the predicted instance and its ground truth counterpart is less than a predefined threshold. For our experiments, we set these thresholds at 0.5, 1.0, and 1.5 meters.

**Implementation Details.** Our model leverages 8 NVIDIA RTX 3090 GPUs for training. We adopt AdamW [25] as the optimizer and utilize Cosine Annealing with a linear warm-up phase [24] as the learning rate scheduler. For more details on hyperparameters, please refer to supplementary materials. Furthermore, our model operates with two objective configurations: a simplified one that adheres to the losses defined in Equation 8, and a comprehensive one that extends to include depth estimation, as well as PV and BEV segmentation losses, as delineated in Equation 7.

## 4.2. Main Results

**NuScenes.** As delineated in Table 1, our method delivers a state-of-the-art performance, achieving a mean Average Precision (mAP) of 69.4% using a camera-only setup and the ResNet50 [10] backbone. Our approach particularly improves the precision for identifying lane dividers and road boundaries, with enhancements of +1.5% points and +1.7%, respectively. Importantly, these gains in performance do not come at the cost of efficiency, as our method sustains inference speeds on par with the previously established state-of-the-art, measured in frames per second (FPS). Also, our method achieves significantly improved performance with extra LiDAR inputs, which indicates the generalizability of our method to multi-modality settings. Moreover, we also compare performance under different weather conditions, as presented in Table 2. Our method exceeds previous works under sunny, cloudy, and rainy scenarios, which shows the potential of geometry to raise model robustness to varied weather conditions.

**Argoverse 2.** Extending our evaluation to the Argoverse 2 dataset, as presented in Table 3, our method also presents a new SOTA performance of 71.8% mAP, outperforming the highly advanced MapTRv2 model by +4.4%. This achievement not only demonstrates the effectiveness of our approach on a different dataset but also emphasizes the adaptability and precision of our algorithm in the evolving landscape of autonomous driving technologies.

Table 3. Comparison on Argoverse 2 dataset. Our method demonstrates significant performance improvements over previous methods.

Methods	Backbone	Seg. Loss	AP <sub>div</sub> (↑)	AP <sub>ped</sub> (↑)	AP <sub>bnd</sub> (↑)	mAP(↑)	FPS(↑)
VectorMapNet [ICML'23] [21]	R50		36.1	38.3	39.2	37.9	-
GeMap [Ours]	R50		<b>67.6</b> ↑3.1.5	<b>59.3</b> ↑21.0	<b>64.7</b> ↑25.5	<b>63.9</b> ↑26.0	13.5
HDMaPNet [ICRA'22] [14]	EB0	✓	5.7	13.1	37.6	18.8	-
MapTRv2 [Arxiv'23] [19]	R50	✓	72.1	62.9	67.1	67.4	<b>13.6</b>
GeMap [Ours]	R50	✓	<b>75.7</b> ↑3.6	<b>69.2</b> ↑6.3	<b>70.5</b> ↑3.4	<b>71.8</b> ↑4.4	12.1

Table 4. Ablation study on NuScenes datasets. We only train the model for **24 epochs** and use simplified objectives (Equation 8).

Method	$\mathcal{L}_{shp}$ (§ 3.3.1)	$\mathcal{L}_{rel}$ (§ 3.3.2)	GDA (§ 3.5)	AP <sub>div</sub> (↑)	AP <sub>ped</sub> (↑)	AP <sub>bnd</sub> (↑)	mAP(↑)
Baseline				49.5	44.7	53.7	49.3
+ Decoupled Attention			✓	53.4	46.6	53.5	51.2
+ Single Euclidean Loss		✓		51.0	45.4	52.7	49.7
	✓			51.7	43.4	53.0	49.4
+ Euclidean Loss	✓	✓		51.5	43.9	51.1	48.8
+ Single Euclidean Loss with Decoupled Attention	✓		✓	54.0	48.2	53.1	51.8
		✓	✓	<b>54.7</b>	47.3	<b>55.3</b>	52.4
Full	✓	✓	✓	53.6 ↑4.1	<b>49.2</b> ↑4.5	54.8 ↑1.1	<b>52.6</b> ↑3.3

### 4.3. Ablation Study

Ablation studies on the NuScenes dataset are carried out to evaluate the individual contributions of our method’s components and other vision backbones.

**Components Ablation.** The ablation experiments, detailed in Table 4, involved training the model for a reduced duration of 24 epochs with a simplified objective described by Equation 8, to facilitate efficient analysis. These experiments confirm the significant role of GDA, which alone increases mAP by +1.9%. Moreover, applying the full suite of components results in a further mAP enhancement of +1.4%. A notable discovery is the detrimental effect on model performance when Euclidean loss is applied without GDA, which leads to a 0.5% reduction in mAP. This reinforces our position that conventional self-attention mechanisms are insufficient for encoding a variety of geometry.

**Backbone Ablation.** Additionally, we investigate 3 vision backbones, and the results are presented in Table 5. Our method achieves significantly improved performance with more advanced vision backbones. Specifically, VoVNetV2-99 [13] and Swin-Transformer Tiny [22] outperform the ResNet50 baseline by +2.8% and +2.6% on mAP.

Table 5. Ablation of vision backbones on Nuscenes datasets.

Backbone	AP <sub>div</sub> (↑)	AP <sub>ped</sub> (↑)	AP <sub>bnd</sub> (↑)	mAP(↑)	FPS(↑)
R50	69.8	67.1	71.4	69.4	<b>13.3</b>
Swin-T	<b>72.8</b>	70.4	72.8	72.0	10.0
V2-99	72.5	<b>70.7</b>	<b>73.5</b>	<b>72.2</b>	9.5

### 4.4. Visualization Analysis

**More Accurate Shape Perception.** Scenario (a) in Figure 6 demonstrates our method’s capability in accurately identifying complex road boundary shapes, such as an elongated triangular tail—typical in lane merging or diversion

areas. This precise result is attributed to the shape geometry we propose, which allows for a more accurate description of the tail feature, in contrast to the MapTR model, which does not discern it as effectively.

**Alleviating Occlusion Issues.** The scenarios depicted in (b) and (c) of Figure 6 demonstrate the utility of our shape geometry in alleviating challenges associated with occlusions in partially visible instances. In particular, scenario (b) presents a pedestrian crossing whose segment is concealed, necessitating models to hypothesize the hidden geometry based on contextual semantic information. Our method leverages geometry between road boundaries and pedestrian crossings to reconstruct a more faithful representation of the occluded area. Scenario (c) features a black car that obscures part of a pedestrian crossing; nonetheless, our approach successfully deduces the overall structure of the crossing within a complex shape. Contrastingly, MapTR [18] struggles with such complex shape recovery under similar occlusion conditions.

#### Enhanced Robustness to Rotational Transformations.

Scenario (d) in Figure 6 exemplifies the resilience of our method to rotational transformations, as evidenced when the ego-vehicle executes a right turn causing the BEV map to appear highly tilted. Additionally, this scenario features lanes that are extensively obscured by vehicular traffic. Despite these challenges, our approach more adeptly maintains the integrity of lane width and parallelism, which are key geometry, in contrast to the MapTR [18] model. This underscores the superior robustness of our geometric constructs against rotational distortions.



Figure 6. Visualization results. Instances hard to construct are highlighted in orange boxes. Scenario (a) depicts a complex triangular road boundary with an extended tail. Scenarios (b) and (c) depict pedestrian crossings that can only be partially observed. In scenario (d), the BEV map is tilted and lane markings are obscured by vehicles. These challenging cases indicate the superiority and robustness of GeMap.

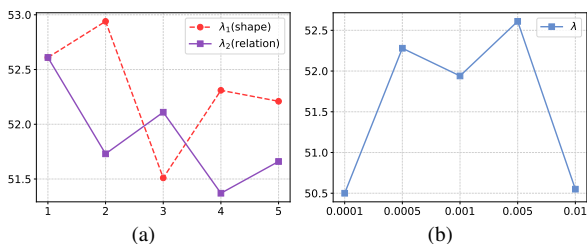


Figure 7. Hyperparameter experiments. (a) Best performance is reached with balanced Euclidean shape and relation losses. (b) Model performances degrade with too large or small  $\lambda$ .

#### 4.5. Hyperparameter Experiments

##### Comparative Impact of Euclidean Loss Components.

Figure 7a shows that our method exhibits larger sensitivity to the Euclidean shape loss than to the relation loss, as evidenced by the steeper change of the performance curve.

The optimal result is obtained when the shape and relation losses are relatively balanced by weights, implying that both contribute comparably to the model’s optimization process.

##### Optimization of Euclidean Loss Weighting.

The performance of the model, as demonstrated in Figure 7b, peaks when the weight of the Euclidean loss,  $\lambda$ , is set to  $5 \times 10^{-3}$ . Notably, model performance degrades with a too large or too small  $\lambda$ , which informed our decision to use a  $\lambda$  value of  $5 \times 10^{-3}$  for our experiments.

## 5. Conclusion

In this paper, we realize significant shape and relation geometry inherent in HD map instances and propose the GeMap. GeMap includes the integration of Euclidean shape and relation losses for auxiliary supervision. To further refine the model’s awareness of diverse geometry, we introduce a geometry-decoupled attention mechanism.



GeMap has achieved state-of-the-art performances on both the NuScenes and Argoverse 2 datasets, underscoring its effectiveness. Despite these promising results, the current application of geometry remains fundamental, and future research could focus on more sophisticated representations or enhanced geometric patterns. Furthermore, the application of geometry extends beyond HD map construction, offering potential solutions to occlusion challenges in other autonomous driving tasks. We anticipate that these findings will inspire further research. **Acknowledgments.** This work was funded by National Natural Science Foundation of China (No. 62272045).

# Online Vectorized HD Map Construction using Geometry

## Supplementary Material

This supplementary material is organized as follows:

- More details on the method design (§ A).
- Further quantitative experimental results (§ B).
- Additional visualization results under three weather conditions (§ C).

### A. Additional Details

#### A.1. Objective Functions

**Two Objective Configurations.** As detailed in § 3.4, our method employs two distinct objective functions. The full objective function is defined as follows:

$$\mathcal{L} = \lambda \cdot \mathcal{L}_{\text{Euc}} + \beta_1 \cdot \mathcal{L}_{\text{cls}} + \beta_2 \cdot \mathcal{L}_{\text{pts}} + \beta_3 \cdot \mathcal{L}_{\text{dir}} + \beta_4 \cdot \mathcal{L}_{\text{seg}} + \beta_5 \cdot \mathcal{L}_{\text{dep}} \quad (12)$$

and the simpler one is

$$\mathcal{L}' = \lambda \cdot \mathcal{L}_{\text{geo}} + \beta_1 \cdot \mathcal{L}_{\text{cls}} + \beta_2 \cdot \mathcal{L}_{\text{pts}} + \beta_3 \cdot \mathcal{L}_{\text{dir}}. \quad (13)$$

**Point Order Agnostic Matching.** In accordance with the methodology proposed by MapTR [18], we employ point order-agnostic matching between predictions and ground truth. In the subsequent formulations, we assume that predictions and ground truth have already been paired.

**Classification Loss.** To enhance the model’s comprehension of the semantics associated with various map instance types, we incorporate the classification task. Let  $\hat{\mathbf{p}} \in \mathbb{R}^{N \times C}$  denote the predicted probabilities, where  $C$  is the number of instance categories. Here,  $\hat{p}_{ic}$  represents the predicted probability of instance  $i$  belonging to category  $c$ . With ground truth labels  $\mathbf{y} \in \{1, \dots, C\}^N$ , the objective function based on focal loss is defined as follows:

$$\mathcal{L}_{\text{cls}} = - \sum_{i=1}^N \sum_{c=1}^C \delta[\mathbf{y}_i = c] \cdot \alpha_c (1 - \hat{p}_{ic})^\gamma \log \hat{p}_{ic} \quad (14)$$

where  $\delta[q] = 1$  if proposition  $q$  is true and  $\delta[q] = 0$  otherwise.

**Point Loss.** For the perception of instance positions, we employ a point loss that evaluates  $L^2$  distances between predicted points and ground truth points, which is specified as

$$\mathcal{L}_{\text{pts}} = \sum_{i=1}^N \sum_{j=1}^{N_v} \|\hat{\mathbf{L}}_j^i - \mathbf{L}_j^i\|_2. \quad (15)$$

**Edge Direction Loss.** To obtain more precise displacement vectors, which are crucial in our G-Representation, we incorporate an edge direction loss. This loss quantifies the cosine similarity between predicted displacement vectors and

their corresponding ground truth vectors. Specifically, the loss is defined as

$$\mathcal{L}_{\text{dir}} = - \sum_{i=1}^N \sum_{j=1}^{N_v} \frac{(\hat{\mathbf{v}}_j^i)^\top \mathbf{v}_j^i}{\|\hat{\mathbf{v}}_j^i\|_2 \cdot \|\mathbf{v}_j^i\|_2}. \quad (16)$$

**Segmentation Loss.** The auxiliary binary segmentation task is valuable for assisting the model in the coarse perception of shape geometry. We integrate a convolutional neural network-based BEV segmentation head with BEV features. Let  $\hat{\mathbf{P}}_{\text{bev}} \in \mathbb{R}^{H' \times W'}$  represent the probability of each grid belonging to the instance area, and  $\mathbf{Y}_{\text{bev}} \in \{0, 1\}^{H' \times W'}$  denote the ground truth. The corresponding objective function is defined as

$$\mathcal{L}_{\text{bev}} = \mathcal{L}_{\text{bce}}(\hat{\mathbf{P}}_{\text{bev}}, \mathbf{Y}_{\text{bev}}) \quad (17)$$

where the binary cross entropy loss  $\mathcal{L}_{\text{bce}}$  is

$$\mathcal{L}_{\text{bce}}(\hat{p}, y) = - \delta[y = 1] \cdot \log \hat{p} - \delta[y = 0] \cdot \log(1 - \hat{p}). \quad (18)$$

We also introduce the auxiliary PV segmentation task, incorporating a shared convolutional neural network head for all views. The ground truth is projected back to the PV space to form the binary mask. Let  $\hat{\mathbf{P}}_{\text{pv}}^k \in \mathbb{R}^{H \times W}$  denote the segmentation results for view  $k$  with corresponding ground truth  $\mathbf{Y}_{\text{pv}}^k \in \{0, 1\}^{H \times W}$ , then the objective function can be expressed as

$$\mathcal{L}_{\text{pv}} = \sum_{k=1}^K \mathcal{L}_{\text{bce}}(\hat{\mathbf{P}}_{\text{pv}}^k, \mathbf{Y}_{\text{pv}}^k). \quad (19)$$

Finally, we obtain the segmentation loss as

$$\mathcal{L}_{\text{seg}} = \beta_{\text{bev}} \cdot \mathcal{L}_{\text{bev}} + \beta_{\text{pv}} \cdot \mathcal{L}_{\text{pv}}. \quad (20)$$

**Depth Estimation Loss.** To enhance depth perception, we replace GKT [2] with LSS [30] when applying the full objective function. Let  $\hat{\mathbf{P}}_{\text{dep}}^k \in \mathbb{R}^{H \times W \times D}$  represent the depth distribution of each grid estimated by LSS in the PV space of view  $k$ , where  $D$  represents the number of quantified depth buckets. Given the ground truth  $\mathbf{Y}_{\text{dep}}^k \in \{1, \dots, D\}^{H \times W \times D}$ , the depth estimation loss is defined as

$$\mathcal{L}_{\text{dep}} = - \sum_{k=1}^K \sum_{d=1}^D \delta[\mathbf{Y}_{\text{dep}}^k = d] \cdot \log \hat{\mathbf{P}}_{\text{dep}}^k. \quad (21)$$

## A.2. Hyperparameter Settings

In the default optimization setting, we set the dropout rate to 0.1 and weight decay to 0.03. The first 500 iterations involve a linear warm-up, starting from 1/3 of the maximum learning rate. In the Cosine Annealing scheduler, the minimum learning rate is set to 0.001 of the maximum. Unless explicitly stated otherwise, we train our model for 110 epochs on NuScenes and 24 epochs on Argoverse 2. For the simplified objective configuration, we set the maximum learning rate to  $6 \times 10^{-4}$  with a batch size of 4. When LiDAR input is utilized, the batch size is reduced to 3. In the full objective configuration, varied hyperparameters are detailed in Table A2. Also, the default hyperparameter settings for objective functions are presented in Table A1.

Table A1. Hyperparameters of objective functions.

Parameter	$\alpha_c$	$\gamma$	$\lambda$	$\beta_1$	$\beta_2$
Value	0.25	2	0.005	2	5
Parameter	$\beta_3$	$\beta_4$	$\beta_5$	$\beta_{bev}$	$\beta_{pv}$
Value	0.005	1	3	1	2

Table A2. Hyperparameters under different vision backbones.

Backbone	Max Learning Rate	Batchsize
R50	$6 \times 10^{-4}$	4
V2-99	$6 \times 10^{-4}$	3
Swin-T	$4 \times 10^{-4}$	3

Moreover, we set the number of instance queries as  $N = 50$  and the number of point queries as  $N_v = 20$ . We employ a single layer of encoder in GKT and incorporate 6 attention blocks in the geometry-decoupled decoder. In the context of LSS transformation, the depth spans from 1 to 35 meters, quantified at intervals of 0.5 meters, resulting in  $D = 68$ .

## B. More Experimental Results

In this section, we present additional ablation studies and hyperparameter experiment results. In all of these experiments, the model is trained for 24 epochs on NuScenes using the simplified objective function. Unless otherwise specified, we employ the default settings outlined in § A.2.

### B.1. Decoupled Attention

In the proposed GDA, we decouple shape and relative perception, sequentially applying Euclidean shape and relation attention. For further ablation, we also experiment with naively doubling self-attention layers in one block, denoted as 2-SA. As shown in Table A3, the results indicate the superiority of GDA when cooperating with Euclidean Loss. This outcome is also suggested by the results in § B.2, as

naively increasing the number of attention blocks does not lead to an improvement in the model’s performance. The decoupling of the processing of shape and relation geometry plays a crucial role in our design.

Table A3. GDA collaborates more effectively with Euclidean loss than two layers of vanilla self-attention.

Attention	$AP_{div}(\uparrow)$	$AP_{ped}(\uparrow)$	$AP_{bnd}(\uparrow)$	mAP( $\uparrow$ )
2-SA	53.5	46.2	54.4	51.4
GDA	<b>53.6</b>	<b>49.6</b>	<b>54.7</b>	<b>52.6</b>

### B.2. Impact of the Decoder Block Number

We evaluate the impact of decoder block numbers on the model performance, as presented in Table A4. When increasing the number of blocks from 1 to 6, the mAP increases by +20.8%. However, naively adding more blocks might be detrimental to model performance. For example, mAP decreases by  $-4.7\%$  when increasing the number of blocks from 6 to 12.

Table A4. Impact of the decoder block number. The default setting utilized in our experiments is highlighted in gray.

# Blk.	$AP_{div}(\uparrow)$	$AP_{ped}(\uparrow)$	$AP_{bnd}(\uparrow)$	mAP( $\uparrow$ )
1	33.5	24.7	37.3	31.8
2	42.1	38.9	48.2	43.1
4	51.1	43.5	53.9	49.5
6	53.6	<b>49.2</b>	<b>54.8</b>	<b>52.6</b>
8	<b>54.5</b>	46.4	53.4	51.4
10	52.4	45.7	53.5	50.5
12	49.6	45.1	48.9	47.9

### B.3. Impact of the Query Number

We also evaluate the influence of query numbers on model performance, as detailed in Table A5 for instance queries and Table A6 for point queries.

**Instance Queries.** As depicted in Table A5, augmenting the number of instance queries could be advantageous for the model’s performance. More specifically, the mAP exhibits an increment of +2.2% when the query number is elevated from 50 to 100. This observation aligns with intuition, as a higher number of instance queries implies a broader pool of diverse candidates. Though a larger number of instance queries might be beneficial, we set  $N = 50$  in our major experiments to align with the parameters employed in prior studies [18, 31], ensuring a fairer comparison.

**Point Queries.** It is observed from Table A6 that an excess or insufficient number of point queries has an adverse impact on the model performance. Notably, an interesting finding is that the optimal query number varies accord-

ing to different instance categories. For example, lane dividers exhibit better performance with  $N_v = 10$ , while pedestrian crossings and road boundaries show optimal results with  $N_v = 20$ . This discrepancy is attributed to the straight shape of lane dividers, whereas pedestrian crossings and road boundaries, characterized by more intricate shapes, benefit from a relatively larger point query number. Hence, the results suggest that adapting point query numbers based on the complexity of instance geometry could further enhance the model performance, which is a topic left for future investigation.

Table A5. Impact of the instance query number.

$N$	$AP_{div}(\uparrow)$	$AP_{ped}(\uparrow)$	$AP_{bnd}(\uparrow)$	mAP( $\uparrow$ )
10	30.2	12.3	31.9	24.8
40	51.0	47.5	53.1	50.5
50	53.6	49.2	54.8	52.6
60	52.6	49.0	55.6	52.4
100	<b>56.2</b>	<b>50.2</b>	<b>57.9</b>	<b>54.8</b>

Table A6. Impact of the point query number.

$N_v$	$AP_{div}(\uparrow)$	$AP_{ped}(\uparrow)$	$AP_{bnd}(\uparrow)$	mAP( $\uparrow$ )
5	49.7	31.4	41.8	41.0
10	<b>53.7</b>	45.9	52.5	50.7
20	53.6	<b>49.2</b>	<b>54.8</b>	<b>52.6</b>
30	50.9	48.3	54.7	51.3
40	50.2	47.9	54.6	50.9

### C. More Visualization Results

We present additional visualization cases under varied weather conditions, as illustrated in Figure A1 to Figure A3. Our method is trained with a ResNet-50 backbone using the simplified objective function.

As illustrated in Figure A1, even in challenging rainy conditions, our method demonstrates more robust results. Particularly in scenario (d) of Figure A1, where the highlighted road boundary and lane divider are heavily occluded by water on the front windshield, our method can still recover the entire instance from observed parts. This showcases the potential of the proposed geometric designs.



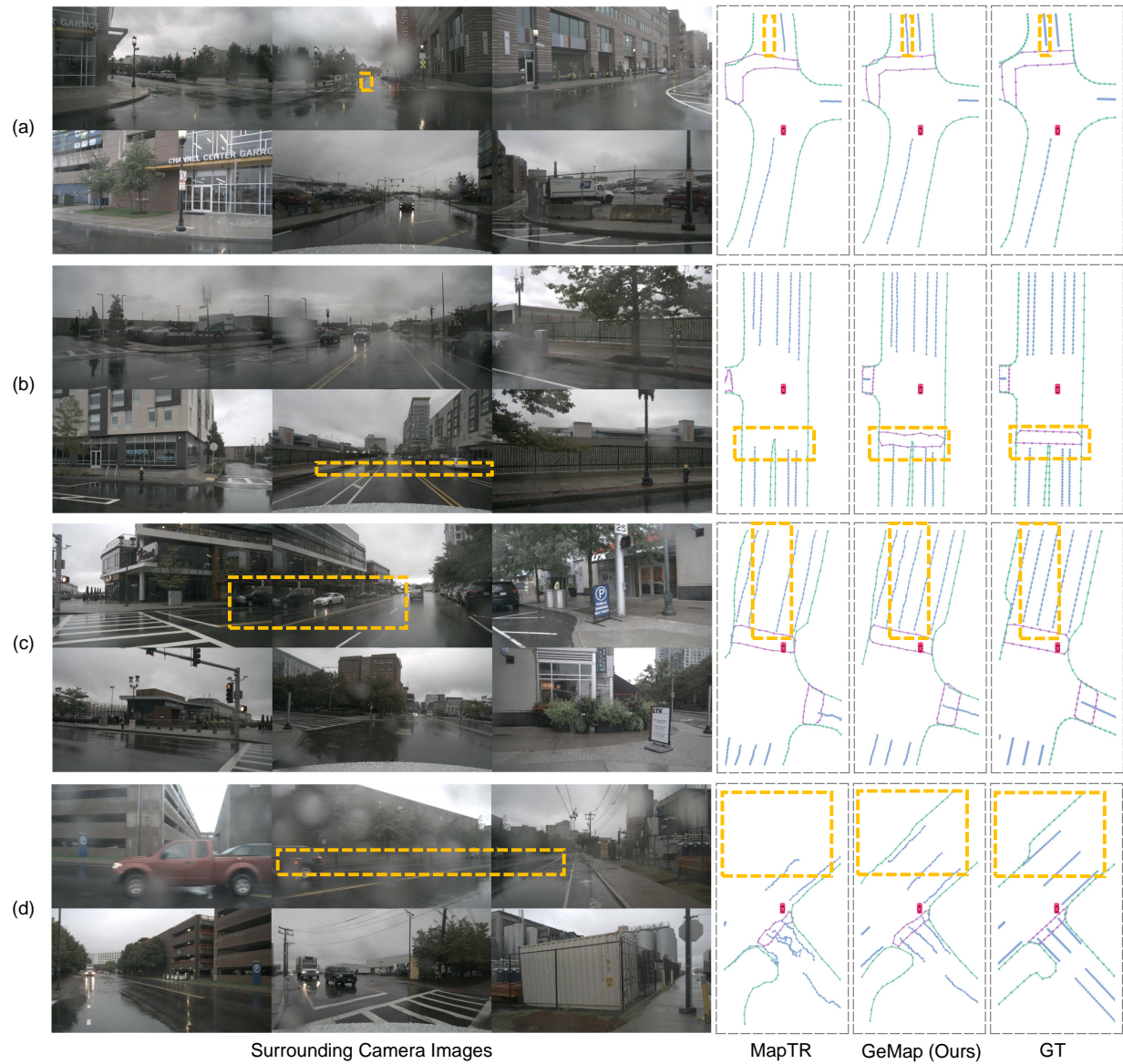


Figure A1. Visualization results under challenging rainy weather conditions. Even with noisy reflections on the road and map instances occluded by water drops, our method still provides robust predictions.

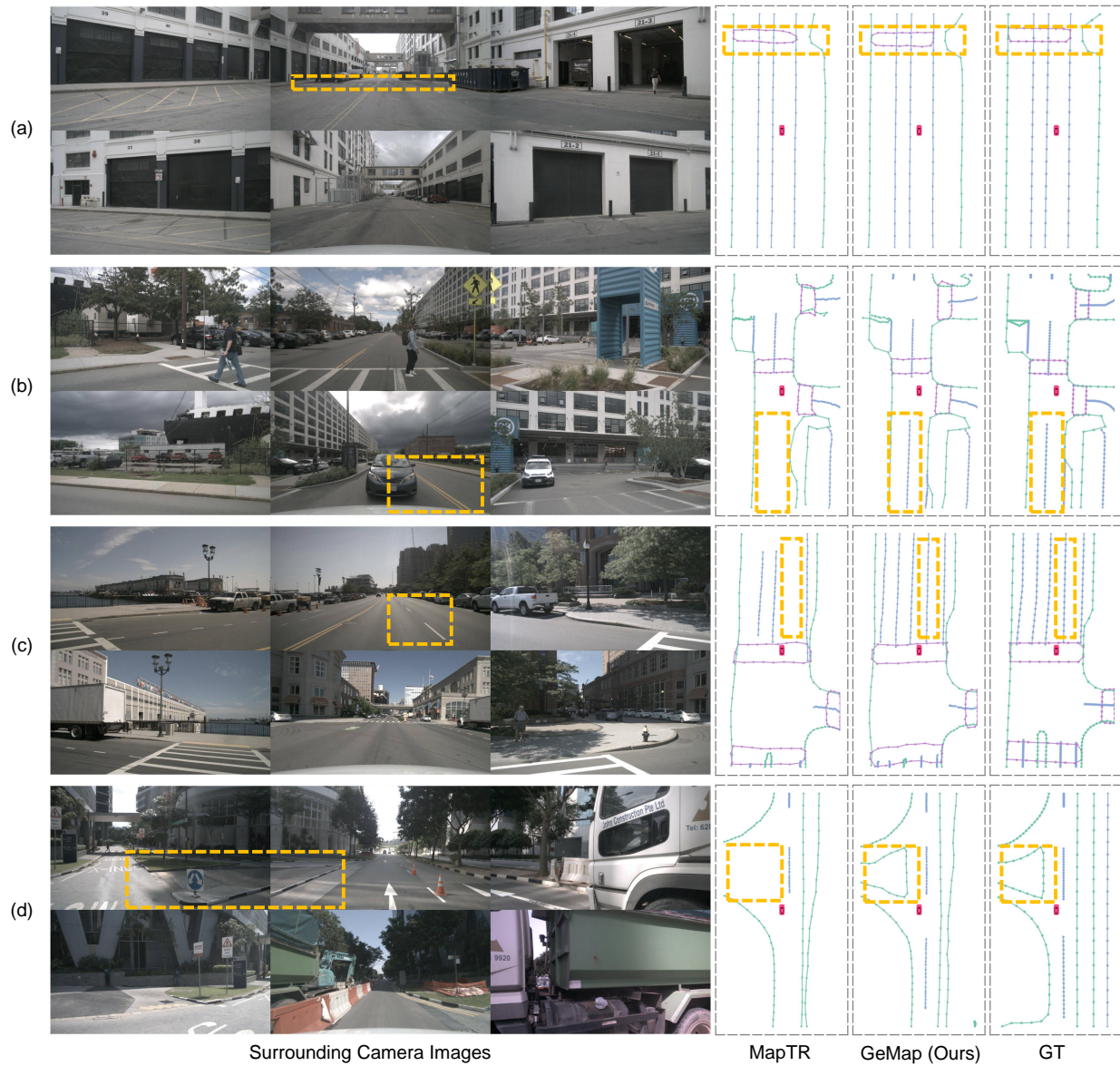


Figure A2. Visualization results under sunny weather conditions.



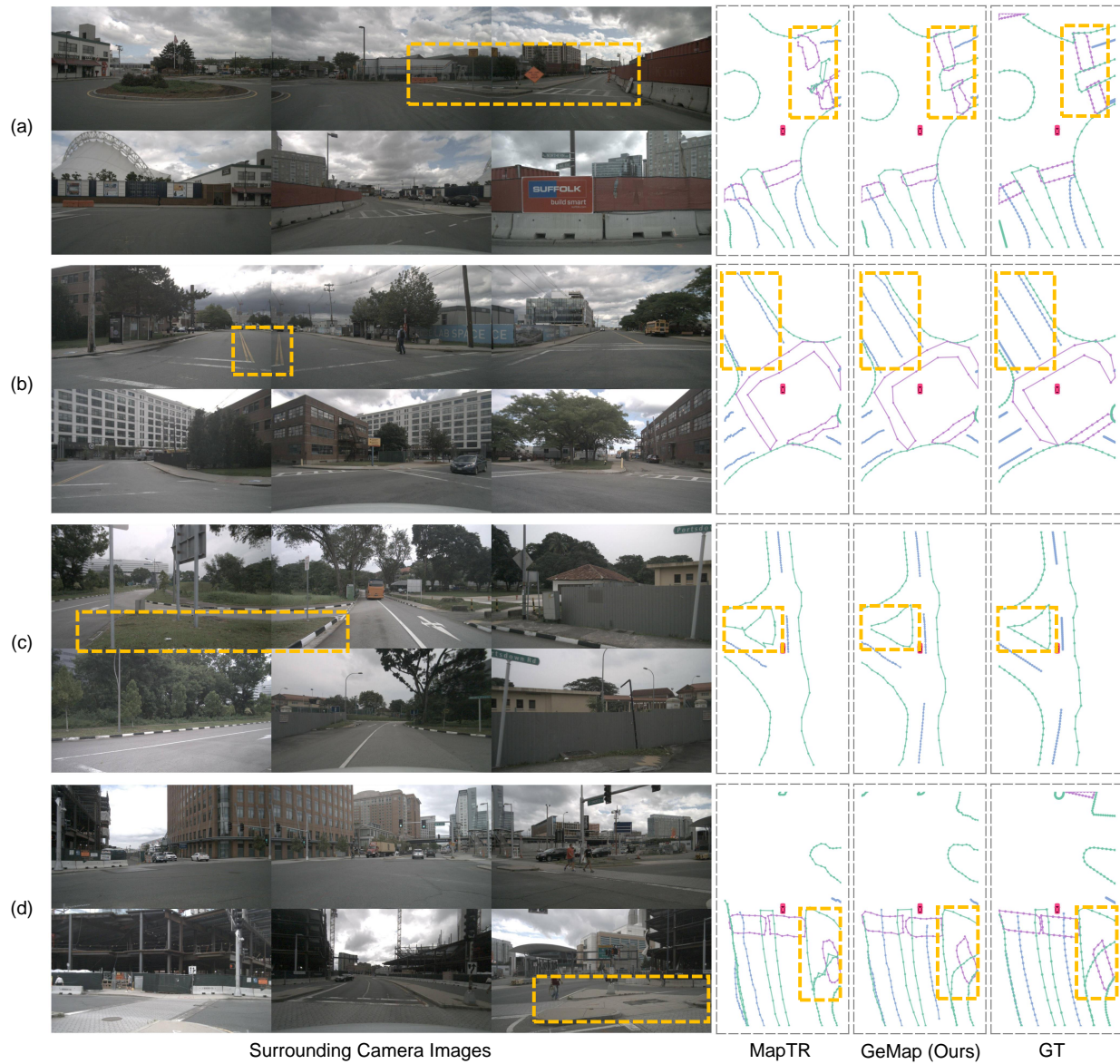


Figure A3. Visualization results under cloudy weather conditions.

## References

- [1] Holger Caesar, Varun Bankiti, Alex H Lang, Sourabh Vora, Venice Erin Liong, Qiang Xu, Anush Krishnan, Yu Pan, Giancarlo Baldan, and Oscar Beijbom. nuscenes: A multi-modal dataset for autonomous driving. In *Proceedings of the IEEE/CVF conference on computer vision and pattern recognition*, pages 11621–11631, 2020. 5
- [2] Shaoyu Chen, Tianheng Cheng, Xinggang Wang, Wenming Meng, Qian Zhang, and Wenyu Liu. Efficient and robust 2d-to-bev representation learning via geometry-guided kernel transformer. *arXiv preprint arXiv:2206.04584*, 2022. 3, 4, 10
- [3] Nachiket Deo, Eric Wolff, and Oscar Beijbom. Multimodal trajectory prediction conditioned on lane-graph traversals. In *Conference on Robot Learning*, pages 203–212. PMLR, 2022. 1
- [4] Wenjie Ding, Limeng Qiao, Xi Qiu, and Chi Zhang. Pivotnet: Vectorized pivot learning for end-to-end hd map construction. In *Proceedings of the IEEE/CVF International Conference on Computer Vision*, pages 3672–3682, 2023. 1, 3, 6
- [5] Jose Luis Vazquez Espinoza, Alexander Liniger, Wilko Schwarting, Daniela Rus, and Luc Van Gool. Deep interactive motion prediction and planning: Playing games with motion prediction models. In *Learning for Dynamics and Control Conference*, pages 1006–1019. PMLR, 2022. 1
- [6] Zhengyang Feng, Shaohua Guo, Xin Tan, Ke Xu, Min Wang, and Lizhuang Ma. Rethinking efficient lane detection via curve modeling. In *Proceedings of the IEEE/CVF Conference on Computer Vision and Pattern Recognition*, pages 17062–17070, 2022. 3
- [7] Jiyang Gao, Chen Sun, Hang Zhao, Yi Shen, Dragomir Anguelov, Congcong Li, and Cordelia Schmid. Vectornet: Encoding hd maps and agent dynamics from vectorized representation. In *Proceedings of the IEEE/CVF Conference on Computer Vision and Pattern Recognition*, pages 11525–11533, 2020. 1
- [8] Chongjian Ge, Junsong Chen, Enze Xie, Zhongdao Wang, Lanqing Hong, Huchuan Lu, Zhenguo Li, and Ping Luo. Metabev: Solving sensor failures for 3d detection and map segmentation. In *Proceedings of the IEEE/CVF International Conference on Computer Vision*, pages 8721–8731, 2023. 2
- [9] Junru Gu, Chenxu Hu, Tianyuan Zhang, Xuanyao Chen, Yilun Wang, Yue Wang, and Hang Zhao. Vip3d: End-to-end visual trajectory prediction via 3d agent queries. In *Proceedings of the IEEE/CVF Conference on Computer Vision and Pattern Recognition*, pages 5496–5506, 2023. 1
- [10] Kaiming He, Xiangyu Zhang, Shaoqing Ren, and Jian Sun. Deep residual learning for image recognition. In *Proceedings of the IEEE conference on computer vision and pattern recognition*, pages 770–778, 2016. 4, 6
- [11] Jialin Jiao. Machine learning assisted high-definition map creation. In *2018 IEEE 42nd Annual Computer Software and Applications Conference (COMPSAC)*, pages 367–373. IEEE, 2018. 1, 2
- [12] Alex H Lang, Sourabh Vora, Holger Caesar, Lubing Zhou, Jiong Yang, and Oscar Beijbom. Pointpillars: Fast encoders for object detection from point clouds. In *Proceedings of the IEEE/CVF conference on computer vision and pattern recognition*, pages 12697–12705, 2019. 6
- [13] Youngwan Lee, Joong-won Hwang, Sangrok Lee, Yuseok Bae, and Jongyoul Park. An energy and gpu-computation efficient backbone network for real-time object detection. In *Proceedings of the IEEE/CVF conference on computer vision and pattern recognition workshops*, pages 0–0, 2019. 7
- [14] Qi Li, Yue Wang, Yilun Wang, and Hang Zhao. Hdmapi: An online hd map construction and evaluation framework. In *2022 International Conference on Robotics and Automation (ICRA)*, pages 4628–4634. IEEE, 2022. 1, 2, 6, 7
- [15] Yinhao Li, Zheng Ge, Guanyi Yu, Jinrong Yang, Zengran Wang, Yukang Shi, Jianjian Sun, and Zeming Li. Bevdepth: Acquisition of reliable depth for multi-view 3d object detection. In *Proceedings of the AAAI Conference on Artificial Intelligence*, pages 1477–1485, 2023. 3
- [16] Zhiqi Li, Wenhao Wang, Hongyang Li, Enze Xie, Chonghao Sima, Tong Lu, Yu Qiao, and Jifeng Dai. Bevformer: Learning bird’s-eye-view representation from multi-camera images via spatiotemporal transformers. In *European conference on computer vision*, pages 1–18. Springer, 2022. 1, 2, 3
- [17] Ming Liang, Bin Yang, Rui Hu, Yun Chen, Renjie Liao, Song Feng, and Raquel Urtasun. Learning lane graph representations for motion forecasting. In *Computer Vision—ECCV 2020: 16th European Conference, Glasgow, UK, August 23–28, 2020, Proceedings, Part II 16*, pages 541–556. Springer, 2020. 1
- [18] Bencheng Liao, Shaoyu Chen, Xinggang Wang, Tianheng Cheng, Qian Zhang, Wenyu Liu, and Chang Huang. MapTR: Structured modeling and learning for online vectorized HD map construction. In *The Eleventh International Conference on Learning Representations*, 2023. 1, 3, 5, 6, 7, 10, 11
- [19] Bencheng Liao, Shaoyu Chen, Yunchi Zhang, Bo Jiang, Qian Zhang, Wenyu Liu, Chang Huang, and Xinggang Wang. Maptrv2: An end-to-end framework for online vectorized hd map construction. *arXiv preprint arXiv:2308.05736*, 2023. 1, 5, 6, 7
- [20] Tsung-Yi Lin, Priya Goyal, Ross Girshick, Kaiming He, and Piotr Dollár. Focal loss for dense object detection. In *Proceedings of the IEEE international conference on computer vision*, pages 2980–2988, 2017. 5
- [21] Yicheng Liu, Tianyuan Yuan, Yue Wang, Yilun Wang, and Hang Zhao. Vectormapnet: End-to-end vectorized hd map learning. In *International Conference on Machine Learning*, pages 22352–22369. PMLR, 2023. 1, 3, 6, 7
- [22] Ze Liu, Yutong Lin, Yue Cao, Han Hu, Yixuan Wei, Zheng Zhang, Stephen Lin, and Baining Guo. Swin transformer: Hierarchical vision transformer using shifted windows. In *Proceedings of the IEEE/CVF international conference on computer vision*, pages 10012–10022, 2021. 7
- [23] Zhijian Liu, Haotian Tang, Alexander Amini, Xinyu Yang, Huizi Mao, Daniela L Rus, and Song Han. Bevfusion:



- Multi-task multi-sensor fusion with unified bird’s-eye view representation. In *2023 IEEE International Conference on Robotics and Automation (ICRA)*, pages 2774–2781. IEEE, 2023. 3
- [24] Ilya Loshchilov and Frank Hutter. Sgdr: Stochastic gradient descent with warm restarts. *arXiv preprint arXiv:1608.03983*, 2016. 6
- [25] Ilya Loshchilov and Frank Hutter. Decoupled weight decay regularization. *arXiv preprint arXiv:1711.05101*, 2017. 6
- [26] Abdelhak Loukkal, Yves Grandvalet, Tom Drummond, and You Li. Driving among flatmobiles: Bird-eye-view occupancy grids from a monocular camera for holistic trajectory planning. In *Proceedings of the IEEE/CVF Winter Conference on Applications of Computer Vision*, pages 51–60, 2021. 2
- [27] Chenyang Lu, Marinus Jacobus Gerardus van de Molengraft, and Gijs Dubbelman. Monocular semantic occupancy grid mapping with convolutional variational encoder–decoder networks. *IEEE Robotics and Automation Letters*, 4(2):445–452, 2019. 1
- [28] Lu Mi, Hang Zhao, Charlie Nash, Xiaohan Jin, Jiyang Gao, Chen Sun, Cordelia Schmid, Nir Shavit, Yuning Chai, and Dragomir Anguelov. Hdmapgen: A hierarchical graph generative model of high definition maps. In *Proceedings of the IEEE/CVF Conference on Computer Vision and Pattern Recognition*, pages 4227–4236, 2021. 2
- [29] Bowen Pan, Jiankai Sun, Ho Yin Tiga Leung, Alex Andonian, and Bolei Zhou. Cross-view semantic segmentation for sensing surroundings. *IEEE Robotics and Automation Letters*, 5(3):4867–4873, 2020. 2
- [30] Jonah Philion and Sanja Fidler. Lift, splat, shoot: Encoding images from arbitrary camera rigs by implicitly unprojecting to 3d. In *Computer Vision—ECCV 2020: 16th European Conference, Glasgow, UK, August 23–28, 2020, Proceedings, Part XIV 16*, pages 194–210. Springer, 2020. 1, 2, 3, 10
- [31] Limeng Qiao, Wenjie Ding, Xi Qiu, and Chi Zhang. End-to-end vectorized hd-map construction with piecewise bezier curve. In *Proceedings of the IEEE/CVF Conference on Computer Vision and Pattern Recognition*, pages 13218–13228, 2023. 1, 3, 5, 6, 11
- [32] Oliver Scheel, Luca Bergamini, Maciej Wolczyk, Błażej Osiński, and Peter Ondruska. Urban driver: Learning to drive from real-world demonstrations using policy gradients. In *Conference on Robot Learning*, pages 718–728. PMLR, 2022. 1
- [33] Lucas Tabelini, Rodrigo Berriel, Thiago M Paixao, Claudine Badue, Alberto F De Souza, and Thiago Oliveira-Santos. Keep your eyes on the lane: Real-time attention-guided lane detection. In *Proceedings of the IEEE/CVF conference on computer vision and pattern recognition*, pages 294–302, 2021. 3
- [34] Lucas Tabelini, Rodrigo Berriel, Thiago M Paixao, Claudine Badue, Alberto F De Souza, and Thiago Oliveira-Santos. Polylnenet: Lane estimation via deep polynomial regression. In *2020 25th International Conference on Pattern Recognition (ICPR)*, pages 6150–6156. IEEE, 2021. 3
- [35] Mingxing Tan and Quoc Le. Efficientnet: Rethinking model scaling for convolutional neural networks. In *International conference on machine learning*, pages 6105–6114. PMLR, 2019. 6
- [36] Wouter Van Gansbeke, Bert De Brabandere, Davy Neven, Marc Proesmans, and Luc Van Gool. End-to-end lane detection through differentiable least-squares fitting. In *Proceedings of the IEEE/CVF International Conference on Computer Vision Workshops*, pages 0–0, 2019. 3
- [37] Ashish Vaswani, Noam Shazeer, Niki Parmar, Jakob Uszkoreit, Llion Jones, Aidan N Gomez, Łukasz Kaiser, and Illia Polosukhin. Attention is all you need. *Advances in neural information processing systems*, 30, 2017. 2
- [38] Jinsheng Wang, Yinchao Ma, Shaofei Huang, Tianrui Hui, Fei Wang, Chen Qian, and Tianzhu Zhang. A keypoint-based global association network for lane detection. In *Proceedings of the IEEE/CVF Conference on Computer Vision and Pattern Recognition*, pages 1392–1401, 2022. 3
- [39] Benjamin Wilson, William Qi, Tanmay Agarwal, John Lambert, Jagjeet Singh, Siddhesh Khandelwal, Bowen Pan, Ratnesh Kumar, Andrew Hartnett, Jhony Kaesemodel Pontes, et al. Argoverse 2: Next generation datasets for self-driving perception and forecasting. *arXiv preprint arXiv:2301.00493*, 2023. 6
- [40] Ziyang Xie, Ziqi Pang, and Yu-Xiong Wang. Mv-map: Off-board hd-map generation with multi-view consistency. In *Proceedings of the IEEE/CVF International Conference on Computer Vision*, pages 8658–8668, 2023. 2
- [41] Yan Yan, Yuxing Mao, and Bo Li. Second: Sparsely embedded convolutional detection. *Sensors*, 18(10):3337, 2018. 6
- [42] Weixiang Yang, Qi Li, Wenxi Liu, Yuanlong Yu, Yuexin Ma, Shengfeng He, and Jia Pan. Projecting your view attentively: Monocular road scene layout estimation via cross-view transformation. In *Proceedings of the IEEE/CVF conference on computer vision and pattern recognition*, pages 15536–15545, 2021. 1
- [43] Tianyuan Yuan, Yicheng Liu, Yue Wang, Yilun Wang, and Hang Zhao. Streammapnet: Streaming mapping network for vectorized online hd map construction. *arXiv preprint arXiv:2308.12570*, 2023. 3, 5
- [44] Gongjie Zhang, Jiahao Lin, Shuang Wu, Yilin Song, Zhipeng Luo, Yang Xue, Shijian Lu, and Zuoguan Wang. Online map vectorization for autonomous driving: A rasterization perspective. *arXiv preprint arXiv:2306.10502*, 2023. 3
- [45] Brady Zhou and Philipp Krähenbühl. Cross-view transformers for real-time map-view semantic segmentation. In *Proceedings of the IEEE/CVF conference on computer vision and pattern recognition*, pages 13760–13769, 2022. 2
- [46] Zikang Zhou, Luyao Ye, Jianping Wang, Kui Wu, and Kejie Lu. Hivt: Hierarchical vector transformer for multi-agent motion prediction. In *Proceedings of the IEEE/CVF Conference on Computer Vision and Pattern Recognition*, pages 8823–8833, 2022. 1
- [47] Xizhou Zhu, Weijie Su, Lewei Lu, Bin Li, Xiaogang Wang, and Jifeng Dai. Deformable detr: Deformable transformers for end-to-end object detection. *arXiv preprint arXiv:2010.04159*, 2020. 4